

Superior Stable Self-Healing SnP_3 Anode for Sodium-Ion Batteries

Xiulin Fan, Jianfeng Mao, Yujie Zhu, Chao Luo, Liumin Suo, Tao Gao, Fudong Han, Sz-Chian Liou, and Chunsheng Wang*

Lithium-ion batteries have been extensively employed as energy sources for portable electronics, and are promising energy storage for electric vehicles and smart grid.^[1] However, the high cost and limited availability of lithium resources restrict the lithium-ion batteries for sustainable and cost-efficient large-scale applications.^[2] Owing to low cost, abundant availability of sodium, sodium-ion batteries (SIBs) have recently attracted much attention.^[3,4] Yet, the energy density of sodium-ion batteries is still lower than that of Li-ion batteries.^[5] Extensive efforts have been devoted to developing high-capacity anode materials.^[6] It has been demonstrated that Sn ,^[7,8] Sb ,^[4,9,10] SnSb ,^[11,12] Pb ,^[13] P ^[14–18] can alloy with Na to deliver much higher capacity ($400\text{--}1800\text{ mA h g}^{-1}$) than carbon materials ($100\text{--}300\text{ mA h g}^{-1}$) in Na-ion batteries.^[19] However, such an alloying reaction is also accompanied with huge volume expansion of the host materials (525% volume increase from Sn to $\text{Na}_{15}\text{Sn}_4$,^[20] and 490% from P to Na_3P),^[14] resulting in continuous and accumulated pulverization, and then a fast capacity decay. Qian et al.^[14] reported that an amorphous phosphorus/carbon composite could deliver an initial capacity of 1800 mA h g^{-1} at a current density of 263 mA g^{-1} but the capacity quickly declines to 30% of initial capacity (600 mA h g^{-1}) after 140 cycles. Similarly, Kim et al. also reported that amorphous phosphorus/carbon composites can maintain capacity of 1890 mA h g^{-1} only for 30 cycles at a current density of 143 mA g^{-1} .^[15] Mixing red phosphorus with carbon nanotubes has limited success in improving the cycle stability. The capacity of red P/carbon nanotube composites still quickly decays from initial 1675 to 1284 mA h g^{-1} in ten cycles.^[16] Chevrier et al.^[21] performed the pioneering theoretical/computational work on the screening the sodiation-ion battery anode materials, and suggested that new strategies and approaches are needed to explore novel Na-ion battery anode materials due to the larger volume of sodium-ion size and more serious volume expansion of materials in sodiation than that in lithiation.

The continuous pulverization of alloy anodes during repeated sodiation/desodiation cycles is the major reason for the faster capacity decay. However, if these elements can form a compound (such as Sn_4P_3) after each Na extraction, the pulverization of these elements can be partially repaired and the accumulation of pulverization can be terminated. Therefore, we can use the reversible conversion reaction ($\text{Sn}_4\text{P}_3 + 9\text{Na} \leftrightarrow 3\text{Na}_3\text{P} + 4\text{Sn}$) to terminate the continuous pulverization and aggregation of Sn in alloy reaction ($4\text{Sn} + 15\text{Na} \leftrightarrow \text{Na}_{15}\text{Sn}_4$) in the sodiation/desodiation cycles. Therefore, the pulverization of Sn and P during alloy process can be partially self-healed (recovered) by the conversion reaction process. The drastic enhancement in cycle stability of $\text{Sn}_4\text{P}_3/\text{C}$ composites compared to individual Sn and P anodes has been reported,^[6,22] where the reversible conversion reaction of Sn_4P_3 during sodiation/desodiation has been identified.^[6] The reversible conversion reaction can only self-heal the pulverization and aggregation induced in followed alloy reaction by recombining the cracked Sn and P back to P–Sn compounds in each cycle to avoid the crack propagation and Sn and P aggregation, thus improving the cycle stability of alloy reaction anodes to the cycling life of conversion reaction anodes with much high capacity.

Since P has much higher capacity (2596 mA h g^{-1}) than Sn (847 mA h g^{-1}), SnP_3 exhibits much higher theoretical mass capacity (1616 mA h g^{-1}) than reported Sn_4P_3 (1133 mA h g^{-1}), the highest volumetric capacity of 6890 mA g cm^{-3} among the reported anode materials for SIBs (Figure 1 and Table S1, Supporting Information). Due to the self-healing mechanism through conversion reaction, SnP_3 should also have much better cycling stability than P and Sn anodes. Herein, for the first time, we reported a novel self-healing SnP_3 anode for the SIBs. The SnP_3/C composites synthesized by simple ball milling deliver a high capacity of 810 mA h g^{-1} at current density of 150 mA g^{-1} over 150 cycles without noticeable capacity decay, and retain a high capacity of $\sim 400\text{ mA h g}^{-1}$ even at 2560 mA g^{-1} current density. The SnP_3 shows comparable cycling stability to and higher capacity than reported Sn_4P_3 ($460\text{--}718\text{ mA h g}^{-1}$) at the similar current (100 mA g^{-1})^[6,22,23] but much better cycling stability than P/C composites,^[14,15] and Sn .^[7,8] The reversibility of conversion reaction was confirmed by the formation of SnP_3 after fully desodiation, which partially repaired the pulverization of Sn and P during the alloy process. The self-healing mechanism of SnP_3 offers a new direction to explore superior anode materials for SIBs.

SnP_3/C composites were synthesized by reactive ball milling of Sn, red phosphorus, and carbon black mixtures. In the initial ball milling process, the Sn will react with P to form the brittle

Dr. X. Fan, Dr. J. Mao, Dr. Y. Zhu, C. Luo, Dr. L. Suo, T. Gao, F. Han, Prof. C. Wang
Department of Chemical and Biomolecular Engineering
University of Maryland
College Park, MD 20742, USA
E-mail: cswang@umd.edu

Dr. S.-C. Liou
Maryland Nanocenter
University of Maryland
College Park, MD 20742, USA



DOI: 10.1002/aenm.201500174

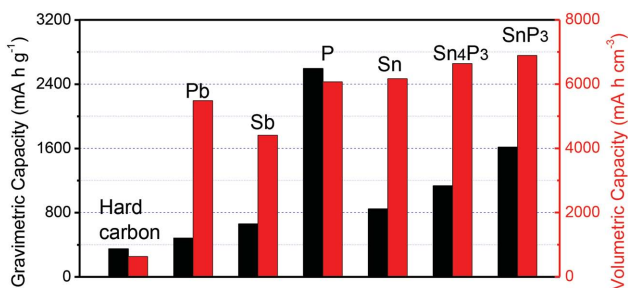


Figure 1. Theoretical gravimetric and volumetric capacities for various anode materials in Na-ion batteries, black bars denote gravimetric capacity, red bars denote volumetric capacity.

SnP₃ and readily fragment into nanometer size, while the ductile carbon black is deformed into lamellae along the (002) planes. These fragmented brittle nanoparticles tend to become occluded by the ductile constituents and trapped in the ductile particles.^[24,25] On further ball milling, the ductile lamellae is convoluted and refined, and uniformly coated on the SnP₃ nanoparticles.^[25,26] The 20 wt% of carbon in SnP₃/C composites is tightly bonded to SnP₃ nanoparticles after ball milling, facilitating electron transfer and stabilizing the solid electrolyte interphase (SEI) layers.

Figure 2 shows the X-ray diffraction (XRD) pattern of the SnP₃/C composite. All of the diffraction peaks in the XRD patterns can be assigned to the SnP₃ (R3m, PDF#23-0970) with rhombohedral lattice structure. No impurities can be detected in the SnP₃/C composite, implying that Sn and P were completely transformed to SnP₃ compound. Broadened diffraction peaks suggest that the SnP₃ is in nanocrystalline scale. The average grain size of SnP₃ in the composite is estimated from the largest peak of (202) using the Scherrer equation ($d = 0.9\lambda/\beta \cos \theta$). The average crystal size of SnP₃ is about 18 nm.

The morphology of the SnP₃/C composite was further investigated by transmission electron microscopy (TEM) and scanning electron microscopy (SEM), as shown in **Figure 3**. The TEM image shows that the secondary SnP₃ compounds with size of tens nanometers agglomerate into micro-sized primary

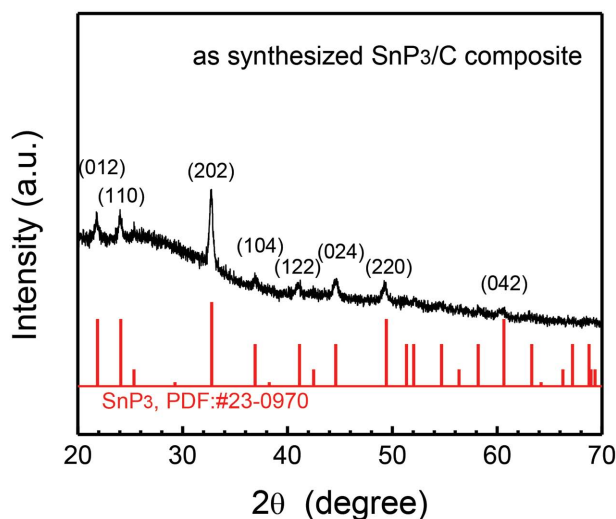


Figure 2. XRD patterns of as-synthesized SnP₃/C composite.

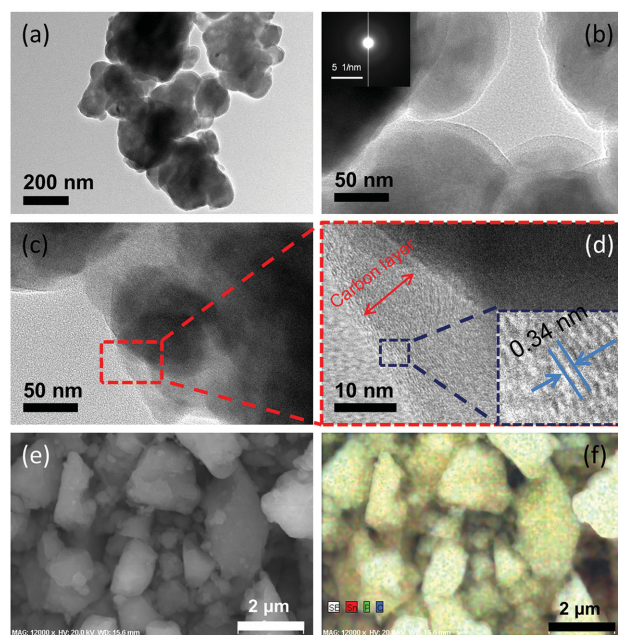


Figure 3. a–d) The TEM and HRTEM images of the as-synthesized SnP₃/C composite; e, f) the SEM and corresponding elemental mapping of Sn, P, and C. The inset in (b) is the corresponding selected area electron diffraction patterns.

particles (Figure 3a,e). The high-resolution TEM image in Figure 3b–d shows that the secondary SnP₃ nanoparticles are uniformly coated by a 10 nm carbon layer (Figure 3b,c). The parallel fringes in the carbon coating layer have the space of ≈ 0.34 nm (Figure 3d), corresponding to the undestroyed (002) planes of graphitic grain. The carbon coating functions as a buffer layer to accommodate the volume change and mechanical stress during Na insertion and extraction. The diffuse selected-area electron diffraction pattern (inset in Figure 3b) indicates that the agglomerates are composed of SnP₃ polycrystallites within several nanometers, in line with the broadening of the XRD patterns. The SEM image (Figure 3e) shows a morphological feature of the primary SnP₃/C composite with size ranging from hundred nanometers to 1–2 μ m. The elemental mapping (Figure 3f) and individual elements distribution (Figure S1, Supporting Information) in SnP₃/C composite are characterized using energy-dispersive spectroscopy (EDS). The uniform color in P, Sn, and C mapping (Figure 3f) confirms the uniform distribution of Sn, P, and C in the composites. The individual elements distribution in Figure S1 (Supporting Information) also demonstrated that P totally coincides with the Sn and also is in the vicinity of carbon, which is consistent with the results of TEM images. The micro-sized primary SnP₃/C composite particles formed by aggregation of nanosized secondary SnP₃ can take advantage of a high tap density and low initial irreversible capacity of microsize primary particle, and short sodium diffusion length and less stress of nanosized secondary SnP₃.

The electrochemical performance of the SnP₃/C for the Na⁺ ion insertion/extraction was evaluated using a half cell with a sodium foil as counter electrode. **Figure 4a** and Figure S2 (Supporting Information) show the cyclic voltammograms (CVs) of

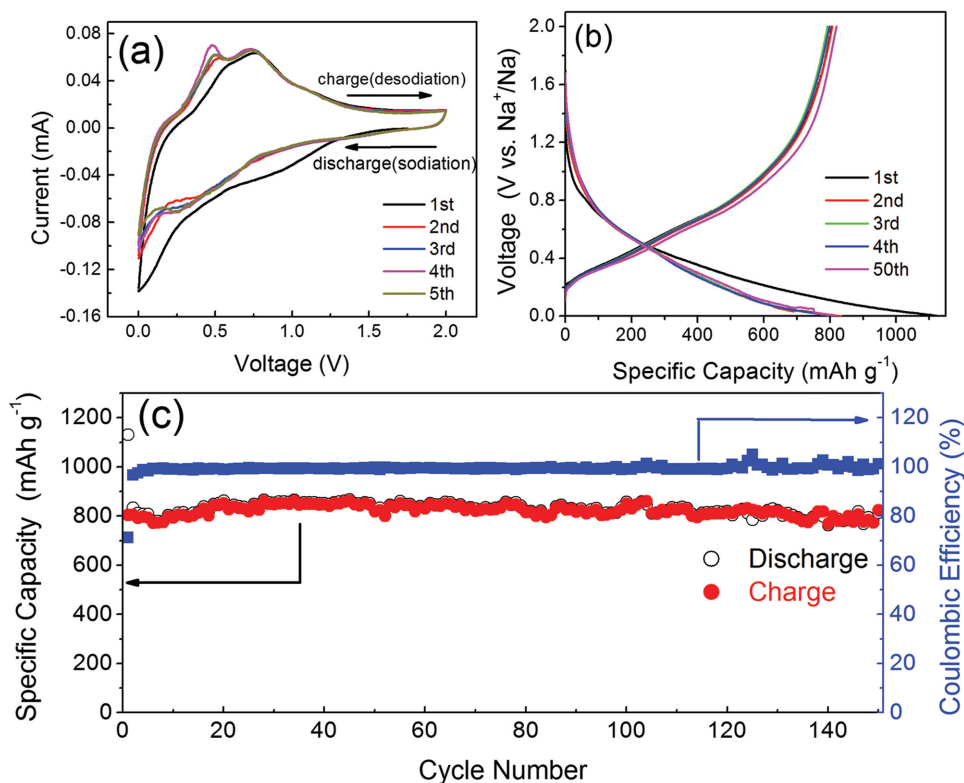


Figure 4. a) CV curves of the SnP_3/C electrode from 2.0 to 0 V versus Na^+/Na at a scan rate of 0.1 mV s^{-1} ; b) representative discharge/charge profiles of the SnP_3/C electrode between 0 and 2.0 V versus Na^+/Na at a current rate of 150 mA g^{-1} ; c) cycling performance of the SnP_3/C electrode at a current rate of 150 mA g^{-1} .

SnP_3/C anode. A broad shoulder peak at about 1.0 V is observed in the first sodiation scan, but disappears in the second sodiation scan. This peak at 1.0 V is attributed to the formation of a solid–electrolyte interface (SEI) film due to irreversible reduction of the electrolyte. The SEI formation peak was also reported in SnSb -porous carbon nanocomposites,^[11,12] Sb-C composites,^[10] and P-C composites.^[14] Upon further sodiation, a large reduction peak at 0.1 V is observed in the first sodiation scan, but it splits into two peaks at 0.3 and 0.1 V after the first sodiation scan, which is due to the activation process and it was also reported in the $\text{Sn}_4\text{P}_3/\text{C}$ anode material.^[6,22,23] By characterizing phase structure of Sn_4P_3 after sodiation to 0.25 and 0.01 V using ex situ XRD, Qian et al.^[23] confirmed that reduction peak at 0.3 V is attributed to formation of Sn and Na_3P and at 0.1 V peak is attributed to alloy of Sn to form $\text{Na}_{15}\text{Sn}_4$. Therefore, the peak at 0.3 V is attributed to the conversion reaction to form Sn and Na_3P (Equation (1)) and the peak at 0.1 V is due to alloy reaction of Sn to form $\text{Na}_{15}\text{Sn}_4$ compounds (Equation (2)). The formation of $\text{Na}_{15}\text{Sn}_4$ and Na_3P after fully sodiation has been confirmed by the XRD patterns in Figures S3 and S4 in the Supporting Information. $\text{Na}_{15}\text{Sn}_4$ and Na_3P peaks are clearly observed in Figures S3 and S4 (Supporting Information) after fully sodiation of SnP_3/C to 0 V, although the peaks are slightly wide and weak due to less SnP_3 loading in the electrode and much smaller grain size of $\text{Na}_{15}\text{Sn}_4$ and Na_3P . In addition, the conversion reaction (reaction (1)) energy was calculated using the Materials Project's reaction calculator.^[27] The calculated -4.05 eV of conversion reaction energy can translate into

a computed voltage of 0.45 V, which perfectly coincides with the sodiation peak of 0.3 V and desodiation peak of 0.65 V in Figure 4a. In the reversed desodiation scans, two large oxidative peaks centered at 0.35 and 0.65 represent dealloying of $\text{Na}_{15}\text{Sn}_4$ and reverse conversion reaction of Na_3P , similar to Sn_4P_3 .^[6,22,23]

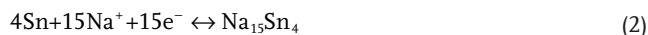


Figure 4b shows the representative discharge/charge profiles of the SnP_3/C composite electrode at a current density of 150 mA g^{-1} . All of the capacities are calculated based on the total mass of SnP_3/C composite, not just on the SnP_3 . The initial sodiation of SnP_3/C composite gives an overall capacity of 1131 mA h g^{-1} (1414 mA h g^{-1} for SnP_3), while 71.2% of inserted Na (805 mA h g^{-1}) can be extracted. The Coulombic efficiency quickly jumps to more than 98% in the second cycles. The reversible capacity of SnP_3/C composite is larger than that of Sn_4P_3 .^[6,22,23] This is because the weight of phosphorous (44 wt%) in SnP_3 material is much higher than that (16 wt%) of P in Sn_4P_3 anode.^[6] The initial Coulombic efficiency of SnP_3/C composite is much higher than that of Sn-related composites.^[7,28] Figure 4c shows the cycling performance of the SnP_3/C composite electrodes at a current rate of 150 mA g^{-1} . SnP_3/C composite can maintain the initial capacity over 150 cycles without noticeable capacity decay. To the best of

our knowledge, SnP_3/C composites reported here show the best cycling performance in all P and Sn–P alloys reported to date for SIBs. The Coulombic efficiency of the electrode is as high as >99% after six cycles, indicating excellent reaction reversibility. SnP_3/C composite shows much better cycling stability than individual P^[14–18] and Sn.^[8] Qian et al. also reported the significant improvement in cycling stability of $\text{Sn}_4\text{P}_3/\text{C}$ comparing to Sn/C and P/C.^[23] The significant enhancement in cycling stability of Sn–P compounds may be attributed to the reversible conversion reaction, which can terminate the continuous pulverization of P and Sn during sodiation/desodiation cycles. However, the reversibility of conversion reaction may be kinetically reduced and the cycling stability of SnP_3/C may become worse if reducing the cutoff potential to <2.0 V (reducing conversion reaction driving force) and increasing cycling current (shorting the conversion reaction times). The cycling stability of SnP_3/C was further evaluated in the much worse protocol by cutting the cycling potential range from 0.0–2.0 V to 0.0–1.2 V and increasing the current from 150 to 400 mA g^{-1} . The representative charge–discharge profiles and the corresponding cycling performance are shown in Figure S5 (Supporting Information). In the first ten cycles, the reversible capacity increased from 475 to 550 mA h g^{-1} , showing an activation process. After the activation process, the SnP_3/C composites exhibit a capacity retention of >92% over 100 cycles compared with the capacity at the tenth cycle, demonstrating robustness for the changes in the current and cutoff potentials. Since FEC in electrolyte can also improve the cycling stability and the superior performance of SnP_3/C was obtained in the electrolyte containing 50% FEC electrolyte. To confirm the good cyclability is from the “self-healing” effect of SnP_3 rather than FEC-rich electrolyte, the electrochemical performance of SnP_3/C materials in FEC-free electrolyte (1.0 M NaClO_4 in EC/DEC) and FEC-low electrolyte (1.0 M NaClO_4 in EC/DEC + 10%FEC) was tested. The cycling performance and the representative cycling curves are shown in Figure S6 (Supporting Information). The SnP_3/C anode still maintains a relatively stable capacity although the FEC content in electrolyte reduces from 50%, 10% to 0.0%. Yet, the Coulombic efficiency of SnP_3/C increases with FEC content in electrolytes. Therefore, the self-healing due to the interaction of Sn and P enhances the capacity retention, while the FEC stabilizes the SEI layers on the surface of the electrode material.

In addition to the supper cycling performance, the SnP_3/C composite also exhibits an impressive rate capability. **Figure 5** shows the rate behavior of the SnP_3/C electrode when the current increases from 0.1 to 3.2 C (80–2560 mA g^{-1}). Here, it is assumed that the capacity of 860 mA h g^{-1} at lowest current of 80 mA g^{-1} is the maximum capacity for the composite. The representative charge–discharge profiles at different currents are presented in Figure S7 (Supporting Information). The electrode delivers reversible capacities of 860, 790, 680, and 570 mA h g^{-1} at a charge–discharge current of 0.1, 0.2, 0.4, and 0.8 C, respectively. Even at high current of 3.2 C, the SnP_3/C electrode can still provide $\approx 400 \text{ mA h g}^{-1}$, which is one of the best performance anodes reported for SIBs. Moreover, when the current density is finally returned to its initial value of 0.1 C, the initial capacity is also completely recovered, implying the excellent tolerance for the rapid sodium ion insertion/extraction cycles.

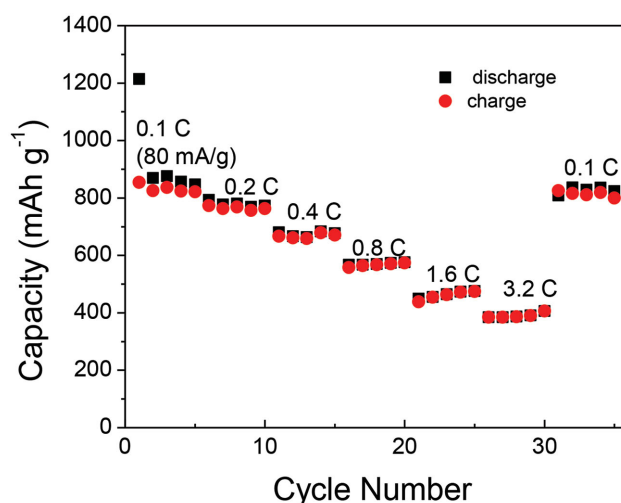


Figure 5. Rate capability of the SnP_3/C electrode at various current values from 0.1 to 3.2 C (80–2560 mA g^{-1} , assuming the capacity at lowest current of 80 mA g^{-1} to be the maximum capacity).

The high reversibility of the conversion reaction was confirmed by analyzing the phases of fully sodiated SnP_3/C to 0 V and fully desodiated SnP_3/C at 2.0 V using XRD, TEM, EDS, SAD, and XPS. Since all the SnP_3 phases after charging to 2 V at a rate of 150 mA g^{-1} are too small (or amorphous) to be detected by XRD (Figure S8, Supporting Information), we reduced the charging and discharging rates to 20 mA g^{-1} and kept at 2 V for 2 d to allow the phases to grow large enough to be easily detected by XRD, TEM, and XPS. Figure S9 (Supporting Information) shows the TEM, HRTEM, and corresponding FFT results of the sodiated (discharged) SnP_3/C composite. Distinct nanoparticles with size of about 10–20 nm dispersed in the composite. HRTEM shows that these nanoparticles are polycrystalline, and can be assigned to the $\text{Na}_{15}\text{Sn}_4$ phase. The smaller crystalline size of the formed $\text{Na}_{15}\text{Sn}_4$ is in good agreement with the significant broadening of the $\text{Na}_{15}\text{Sn}_4$ peaks for XRD (Figures S3 and S4, Supporting Information). Together with the XRD patterns of the sodiated materials (Figures S3 and S4, Supporting Information), it can be confirmed the sodiation of SnP_3 to $\text{Na}_{15}\text{Sn}_4$ and Na_3P . **Figure 6** shows the phases and microstructures of SnP_3/C after fully desodiation. The XRD pattern of the SnP_3/C composite after fully desodiation (Figure 6a) shows several broad and distinct peaks, which can be assigned to the SnP_3 phase. During sodiation and the following desodiation process, the crystalline structure of SnP_3 will decompose and recombine, significantly reducing the crystalline size, thus lowering and broadening of the XRD peaks. Similar phenomena have also been observed in the Sn_4P_3 ,^[6] Cu_2Sb ,^[29] and NiP_3 anode materials.^[30] Figure 6b,c exhibits the SEM and TEM images of the SnP_3/C electrode after desodiation. SEI layers due to the decomposition of FEC-based electrolytes^[11,31] are clearly observed. Smaller nanoparticles can be observed uniformly distributed in the composites. The high-resolution TEM image in Figure 6c clearly shows a lattice fringe of 0.203 nm in dispersed nanoparticles, corresponding to the d -spacing value of the (024) plane of the SnP_3 , confirming the recovery of the SnP_3 compound. The reformation of SnP_3

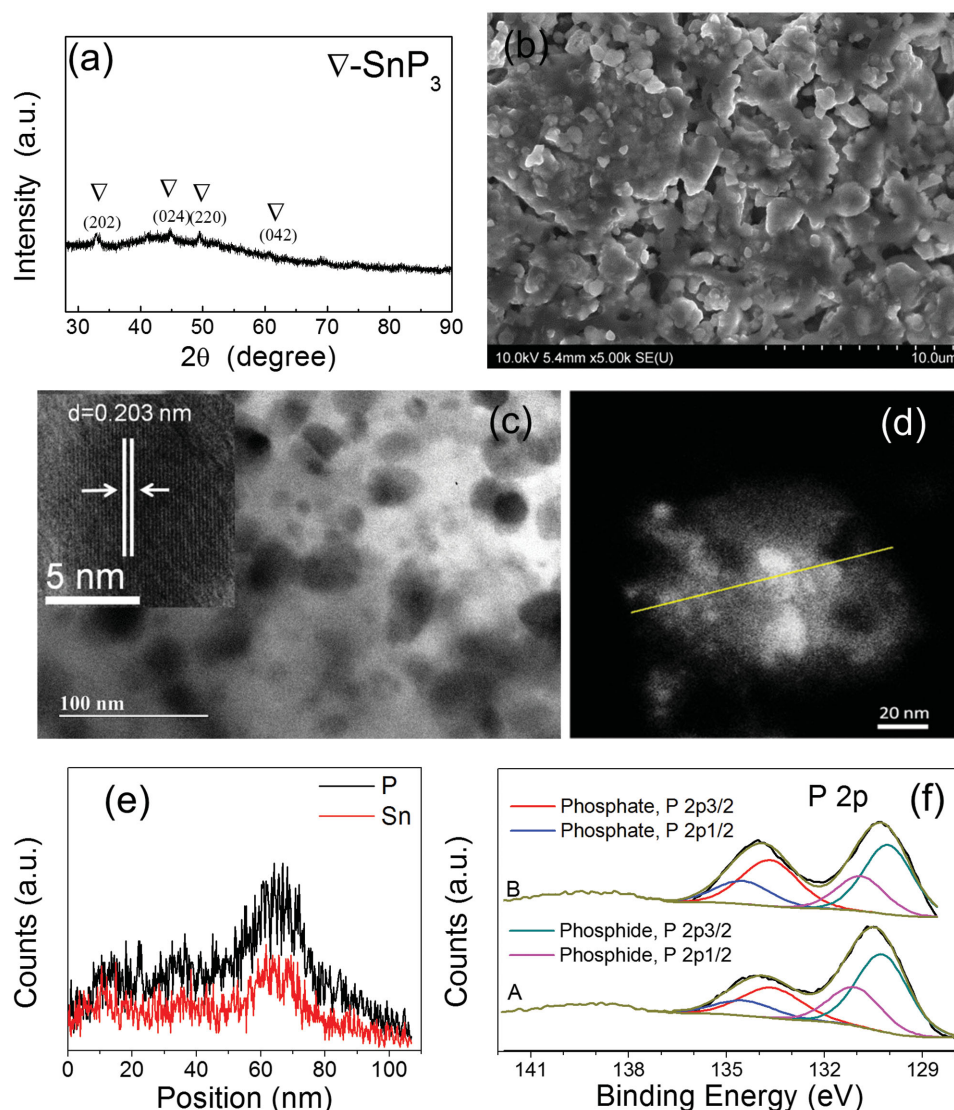


Figure 6. a) XRD pattern of the charged SnP_3/C composite at 20 mA g^{-1} and maintained at 2 V for 2 d ; b) SEM and c) TEM images of SnP_3/C composite after fully charged; d,e) STEM-HAADF image and the corresponding cross-sectional compositional line profiles of Sn and P for the charged SnP_3/C composite; f) comparison of the P2p XPS spectra for the as-synthesized SnP_3/C (A) and charged SnP_3/C (B) composite. The inset of (c) is the HRTEM image of a nanoparticle.

was further supported by the STEM-HAADF image and the corresponding energy-dispersive X-ray spectroscopy (EDS) line profiles, as shown in Figure 6d,e. The intensities of the Sn and P increase in the nanocrystalline (bright) region, and coincide with each other exactly. Besides, the SAD patterns and the EDS mapping results also confirmed the formation of the SnP_3 species, as shown in Figure S10 (Supporting Information). SEM and EDS mapping results (Figure S11, Supporting Information) show the uniform and overlapping distribution of Sn and P in the charged SnP_3/C electrode.

The local atomic environment of the phosphorous species in the composites after full desodiation was also analyzed using XPS and compared with the as-synthesized SnP_3/C composite (Figure 6f). The two peaks at 130.5 and 134 eV can be attributed to the P 2p of phosphide and phosphate, respectively,^[32] both of which can be ideally separated as P 2p_{3/2} and 2p_{1/2} peaks.^[33]

The phosphate peaks indicate the surface of composite is a little sensitive to the oxygen, and oxidation layer on the top surface is formed for the composite in the air. This is quite similar to the phosphorous/graphene composite.^[17] The P2p XPS spectra of fully desodiated SnP_3/C are almost the same as the fresh SnP_3/C , demonstrating the fully reversibility of conversion reaction. The XPS pattern observations in fully desodiated electrode agreed well with the XRD and STEM-HAADF results, and verified the reversible of conversion reaction. The highly reversible conversion reaction was also reported by Kim et al. for Sn_4P_3 anodes.^[6] The reversible conversion reaction (reaction (1)) terminates the pulverization and accumulation in the alloy reaction, although it cannot completely recover the structure of discharged SnP_3 to the structure of the fresh SnP_3 since the conversion reaction only fully recovers the phase but not the structure. However, it is very effective to curb the continuation

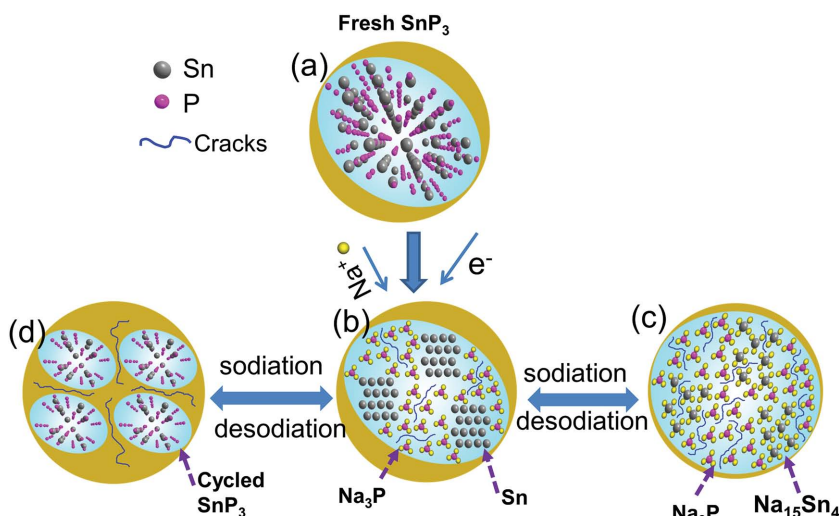


Figure 7. Schematic illustration for the sodiation and desodiation of SnP_3/C composite. Yellow outlayer denotes carbon.

of pulverization in the charge–discharge cycles. The self-healing effect of conversion reaction for alloying anodes is schematically illustrated in **Figure 7**.

In the initial sodiation stage, the crystal SnP_3 (**Figure 7a**) breaks into small composites consisting of nanometric Sn particles dispersed in a small nanocrystalline/amorphous Na_3P matrix through the conversion reaction (**Figure 7b**). Upon further sodiation, Na inserts into Sn to form $\text{Na}_{15}\text{Sn}_4$ through alloying reaction, resulting in pulverization (**Figure 7c**). During the desodiation, the Na first dealloy from $\text{Na}_{15}\text{Sn}_4$ to form Sn and then react with P dealloyed from Na_3P to convert back to SnP_3 with small size (**Figure 7d**), thus healing the cracks of Sn induced in the alloy process and preventing the Sn from aggregation. In the following sodiation/desodiation cycles, the reversible structure changes will take place as illustrated from **Figure 7d,b** to **Figure 7c**; thus, the cracks and aggregation generated in each alloy process will be recovered in the followed reversible reaction process. Even if the conversion reaction is not completely reversible at a high cycling current, the strong bonding between P and Sn will mitigate the aggregation of Sn. Without reversible conversion and strong binding between P and Sn, the pulverization and aggregation of Sn and P particles in the alloy process (**Figure 7b,c**) will be continuously accumulated with charge–discharge cycles, resulting in rapid capacity decay as demonstrated in reported individual Sn and P anodes. The accompanied conversion reaction can improve the cycling stability of alloy anodes to the level of conversion anode, but exhibit much higher capacity than the conversion anodes. In addition to chemical bonding between Sn and P, the Sn generated from conversion reaction is very small, and the Sn particles also provide the electronic channels to activate the electrochemical sodiation reaction of P, while the Na_3P matrix phase (before reverse conversion reaction) can mitigate the aggregation of the Sn particles,^[22] enhancing the rate capability of Sn–P compounds. Finally, SnP_3 successfully takes advantage of the high gravimetric capacity of P, high volumetric capacity of Sn, and favorable conductivity of metallic compound, thus achieving

both high gravimetric capacity and high volumetric capacity.

In summary, we, for the first time, demonstrated the electrochemical performance of SnP_3/C anodes for Na-ion battery. SnP_3/C can reversibly react with Na through conversion and alloy reaction processes. It can provide a high capacity of $\approx 810 \text{ mA h g}^{-1}$ ($\approx 2820 \text{ mA h cm}^{-3}$ for the composite including carbon) at 150 mA g^{-1} , maintain the same capacity for 150 cycles, and can retain 400 mA h g^{-1} even at 2560 mA g^{-1} , which is the best overall performance in all P, Sn, and Sn–P compound anodes for Na-ion batteries reported to date. Detailed analysis using SEM TEM, and XPS revealed that the highly reversible conversion reaction due to strong bonding interaction between Sn and P successfully mitigates the accumulation of pulverization and aggregation for Sn and P, and thus partially self-heals the struc-

ture of SnP_3/C composites and enhances the cycling stability. In addition, the gravimetric and volumetric capacities of SnP_3 composite are also higher than that of Sn_4P_3 due to the high content of P in SnP_3 . The material self-healing of alloy electrodes through conversion reaction may offer a new approach to explore novel superior electrode materials for rechargeable batteries.

Experimental Section

All the chemicals were purchased from Sigma-Aldrich. Before synthesis of the composite, the red phosphorus P was washed with deionized water and ethanol for several times and then dried in vacuum at 70°C for 6 h.

Preparation of SnP_3/C Nanocomposites: SnP_3/C composites were prepared by ball milling under an argon atmosphere. The active materials (Sn and P):carbon black weight ratio was set to 8:2. The Sn:P ratio was 1:3 by molar ratio. The weight ratio of milling balls to powder was 40:1. The rotation speed of the mill was set to 400 rpm for 48 h.

Characterization: The crystalline structure of the active composite was characterized by powder X-ray diffraction (XRD) on a Bruker Smart1000 diffractometer with a Cu $K\alpha$ radiation. The morphology of the sample was investigated by scanning electron microscopy (SEM, Hitachi SU-70) and transmission electron microscopy (TEM, JEM 2100 FEG, 200 keV). X-ray photoelectron spectroscopy (XPS) was conducted on a high sensitivity Kratos AXIS 165 X-ray photoelectron spectrometer with Mg $K\alpha$ radiation. All binding energy values were referenced to the C 1s peak of carbon at 284.6 eV.

Electrochemical Measurements: The charge–discharge performances of the electrode materials were examined by 2032-type coin cells. The SnP_3/C composite was mixed with carbon black and poly-vinyl difluoride (PVDF) dissolved in *N*-methyl-pyrrolidone (NMP) was mixed at a weight ratio of 70:10:20 to form a slurry, which was then pasted on the Cu foil and dried to obtain working electrodes. To test the cycling and rate performance, the loading mass of the active materials for the electrode was about 1 mg cm^{-2} . Pure Na foil was used as counter and reference electrode. The electrochemical performance of the SnP_3/C for the Na^+ ion insertion/deinsertion was investigated in electrolytes of 1 M NaClO_4 in a mixture of fluoroethylene carbonate (FEC) and dimethyl carbonate (DMC) at 1:1 (v/v). All the cells were assembled in a glove box with water/oxygen content lower than 1 ppm and tested at room

temperature. The galvanostatic charge–discharge test was conducted on Arbin battery test station (BT2000, Arbin Instruments, USA). Cyclic voltammetry (CV) testing with voltages ranging from 0 to 2 V under a scan rate of 0.1 mV s^{−1} was recorded using a CHI 600E electrochemical workstation (CH Instruments, Inc., USA).

Supporting Information

Supporting Information is available from the Wiley Online Library or from the author.

Acknowledgements

This work was supported as part of the Nanostructures for Electrical Energy Storage (NEES), an Energy Frontier Research Center funded by the U.S. Department of Energy, Office of Science, Basic Energy Sciences under Award Number DESC0001160. The authors gratefully acknowledge the support of the Maryland NanoCenter and its NispLab. The authors also acknowledge the reviewer's calculation for the reaction energy of the conversion reaction using Materials Project, which exactly matches with our experiment data.

Received: January 24, 2015

Revised: May 24, 2015

Published online: June 26, 2015

- [1] a) R. V. Noorden, *Nature* **2014**, 507, 26; b) J. M. Tarascon, M. Armand, *Nature* **2001**, 414, 359; c) B. Dunn, H. Kamath, J.-M. Tarascon, *Science* **2011**, 334, 928.
- [2] W. Luo, M. Allen, V. Raju, X. Ji, *Adv. Energy Mater.* **2014**, 4, 1400554.
- [3] a) M. D. Slater, D. Kim, E. Lee, C. S. Johnson, *Adv. Funct. Mater.* **2013**, 23, 947; b) B. L. Ellis, L. F. Nazar, *Curr. Opin. Solid State Mater. Sci.* **2012**, 16, 168; c) V. Palomares, P. Serras, I. Villaluenga, K. B. Hueso, J. Carretero-Gonzalez, T. Rojo, *Energy Environ. Sci.* **2012**, 5, 5884.
- [4] Y. Zhu, X. Han, Y. Xu, Y. Liu, S. Zheng, K. Xu, L. Hu, C. Wang, *ACS Nano* **2013**, 7, 6378.
- [5] N. Yabuuchi, K. Kubota, M. Dahbi, S. Komaba, *Chem. Rev.* **2014**, 114, 11636.
- [6] Y. Kim, Y. Kim, A. Choi, S. Woo, D. Mok, N.-S. Choi, Y. S. Jung, J. H. Ryu, S. M. Oh, K. T. Lee, *Adv. Mater.* **2014**, 26, 4139.
- [7] Y. Xu, Y. Zhu, Y. Liu, C. Wang, *Adv. Energy Mater.* **2013**, 3, 128.
- [8] Y. Liu, Y. Xu, Y. Zhu, J. N. Culver, C. A. Lundgren, K. Xu, C. Wang, *ACS Nano* **2013**, 7, 3627.
- [9] a) J. Qian, Y. Chen, L. Wu, Y. Cao, X. Ai, H. Yang, *Chem. Commun.* **2012**, 48, 7070; b) L. Baggetto, P. Ganesh, C.-N. Sun, R. A. Meisner, T. A. Zawodzinski, G. M. Veith, *J. Mater. Chem. A* **2013**, 1, 7985.
- [10] L. Wu, X. Hu, J. Qian, F. Pei, F. Wu, R. Mao, X. Ai, H. Yang, Y. Cao, *Energy Environ. Sci.* **2014**, 7, 323.
- [11] L. Ji, M. Gu, Y. Shao, X. Li, M. H. Engelhard, B. W. Arey, W. Wang, Z. Nie, J. Xiao, C. Wang, J.-G. Zhang, J. Liu, *Adv. Mater.* **2014**, 26, 2901.
- [12] L. Xiao, Y. Cao, J. Xiao, W. Wang, L. Kovarik, Z. Nie, J. Liu, *Chem. Commun.* **2012**, 48, 3321.
- [13] M. Dahbi, N. Yabuuchi, K. Kubota, K. Tokiwa, S. Komaba, *Phys. Chem. Chem. Phys.* **2014**, 16, 15007.
- [14] J. Qian, X. Wu, Y. Cao, X. Ai, H. Yang, *Angew. Chem.* **2013**, 125, 4731.
- [15] Y. Kim, Y. Park, A. Choi, N.-S. Choi, J. Kim, J. Lee, J. H. Ryu, S. M. Oh, K. T. Lee, *Adv. Mater.* **2013**, 25, 3045.
- [16] W.-J. Li, S.-L. Chou, J.-Z. Wang, H.-K. Liu, S.-X. Dou, *Nano Lett.* **2013**, 13, 5480.
- [17] J. Song, Z. Yu, M. L. Gordin, S. Hu, R. Yi, D. Tang, T. Walter, M. Regula, D. Choi, X. Li, A. Manivannan, D. Wang, *Nano Lett.* **2014**, 14, 6329.
- [18] N. Yabuuchi, Y. Matsuura, T. Ishikawa, S. Kuze, J.-Y. Son, Y.-T. Cui, H. Oji, S. Komaba, *ChemElectroChem* **2014**, 1, 580.
- [19] a) D. A. Stevens, J. R. Dahn, *J. Electrochem. Soc.* **2000**, 147, 1271; b) S. Wenzel, T. Hara, J. Janek, P. Adelhelm, *Energy Environ. Sci.* **2011**, 4, 3342; c) S. Komaba, W. Murata, T. Ishikawa, N. Yabuuchi, T. Ozeki, T. Nakayama, A. Ogata, K. Gotoh, K. Fujiwara, *Adv. Funct. Mater.* **2011**, 21, 3859.
- [20] J. W. Wang, X. H. Liu, S. X. Mao, J. Y. Huang, *Nano Lett.* **2012**, 12, 5897.
- [21] V. L. Chevrier, G. Ceder, *J. Electrochem. Soc.* **2011**, 158, A1011.
- [22] W. Li, S.-L. Chou, J.-Z. Wang, J. H. Kim, H.-K. Liu, S.-X. Dou, *Adv. Mater.* **2014**, 26, 4037.
- [23] J. Qian, Y. Xiong, Y. Cao, X. Ai, H. Yang, *Nano Lett.* **2014**, 14, 1865.
- [24] X. Fan, J. Shao, X. Xiao, X. Wang, S. Li, H. Ge, L. Chen, *Nano Energy* **2014**, 9, 196.
- [25] C. Suryanarayana, *Prog. Mater. Sci.* **2001**, 46, 1.
- [26] P. S. Gilman, J. S. Benjamin, *Annu. Rev. Mater. Sci.* **1983**, 13, 279.
- [27] a) A. Jain, G. Hautier, S. P. Ong, C. Moore, C. Fischer, K. Persson, G. Ceder, *Phys. Rev. B: Condens. Matter* **2011**, 84, 045115; b) A. Jain, S. P. Ong, G. Hautier, W. Chen, W. D. Richards, S. Dacek, S. Cholia, D. Gunter, D. Skinner, G. Ceder, K. A. Persson, *Appl. Phys. Lett. Mater.* **2013**, 1, 011002; c) *Materials Project*, <https://www.materialsproject.org/#apps/reactioncalculator> (accessed: March 2015).
- [28] H. Zhu, Z. Jia, Y. Chen, N. Weadock, J. Wan, O. Vaaland, X. Han, T. Li, L. Hu, *Nano Lett.* **2013**, 13, 3093.
- [29] L. Baggetto, K. J. Carroll, H.-Y. Hah, C. Johnson, D. R. Mullins, R. R. Unocic, J. Johnson, Y. S. Meng, G. M. Veith, *J. Phys. Chem. C* **2014**, 118, 7856.
- [30] J. Fullenwarth, A. Darwiche, A. Soares, B. Donnadieu, L. Monconduit, *J. Mater. Chem. A* **2014**, 2, 2050.
- [31] S. Komaba, Y. Matsuura, T. Ishikawa, N. Yabuuchi, W. Murata, S. Kuze, *Electrochem. Commun.* **2012**, 21, 65.
- [32] P. Perez-Romo, C. Potvin, J. M. Manoli, M. M. Chehimi, G. Djéga-Mariadassou, *J. Catal.* **2002**, 208, 187.
- [33] W. M. R. C. D. Wagner, L. E. Davis, J. F. Moulder, G. E. Muilenberg, *Handbook of X-Ray Photoelectron Spectroscopy*, Perkin-Elmer Corporation, Eden Prairie, MN **1979**.